Journal of Materials Chemistry C

Accepted Manuscript

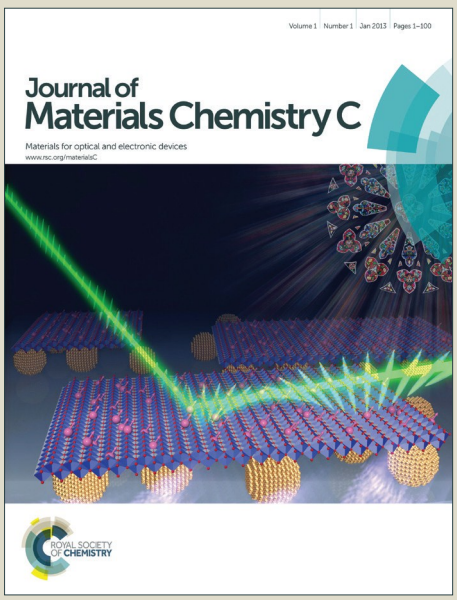

ROYAL SOCIETY OF CHEMISTRY

www.rsc.org/materialsC

Journal Name

ARTICLE TYPE

Cite this: DOI: 10.1039/xxxxxxxxxx

Interatomic Pair Potentials from DFT and Molecular Dynamics for Ca, Ba, and Sr Hexaborides

Kevin M. Schmidt,*[a] Alex B. Buettner,[a] and Victor R. Vasquez[a†]

Received Date
Accepted Date

DOI: 10.1039/xxxxxxxxxx

www.rsc.org/journalname

Alkaline earth hexaborides are thermoelectric materials with unique thermophysical properties that have a broad variety of applications with great potential for new uses in fields such as light-weight armor development, gas storage, and *n*-type thermoelectrics. In this work, we introduce a modeling framework to simulate the basic mechanical behavior of these materials with molecular dynamics. We use a combination of density functional theory, molecular dynamics, and optimization methods to produce a set of interatomic potentials which can describe accurately the equilibrium energetics and mean-square displacements of atoms within these bulk hexaborides. The model works particularly well for hexaborides with large cations.

1 Introduction

Alkaline earth hexaborides (AEB_6) are a subset of the more general class of metal hexaborides (MB_6) containing a divalent metal cation (e.g., Ca, Sr, Ba) located at the central site of a body-centered cubic (BCC) type lattice. Like all other MB_6 compounds, they share in the attractive features of low density, low thermal expansion coefficients, low work functions, chemical inertness, high melting points, and high values of hardness [1–10] and can be synthesized in a variety of ways [7,11–14]. Current practical uses for AEB_6 materials include neutron radiation absorbents, protective surfaces, high temperature structures, and wear-resistant parts [14,15], and present research is aimed at finding new applications (*e.g.,* light-weight armor [16] and *n*-type thermoelectric materials [17]). One of the fascinating features of these materials is their reaction to stoichiometric and structural inhomogeneities. Doping, vacancies, and impurities have been known to reduce work functions and enhance thermionic emission [18], modify lattice parameters [13], promote ferromagnetism [19,20], alter optical properties [21], and affect thermal and electronic conduction [13]. All of these suggest that specific characteristics can be fine-tuned by the proper synthesis methods. Further understanding of these materials at atomic scales is necessary for optimization and applications development, and atomic/molecular modeling methods have great potential to provide fundamental insight in the behavior of these hexaborides.

From a molecular dynamics (MD) perspective, little is known about the fundamental behavior of MB_6 materials at atomic and molecular scales. Most modeling efforts are from density functional theory (DFT), focusing on electronic behavior and electronic properties estimation studies. Applications that involve controlling mass transport and molecular storage require an understanding of the transport mechanisms at molecular scales. It is of particular interest to study how ions move in these materials under the influence of external electrical fields with temperature and pressure gradients. In this work, we propose a MD modeling framework where the boron octahedral units in the MB_6 structure are constrained to their equilibrium volumes but are allowed to move with rigid body dynamics, interacting with inter-octahedral boron atoms and metal ions. We modeled the interatomic interactions using pairwise potentials for inter-octahedral boron-boron, metal-metal, and metal-boron atom pairs. These potentials are developed from a combination of self-consistent DFT calculations and MD simulations linked through a parameter optimization approach to capture the basic fundamental behavior and properties of these hexaboride materials in a MD setting. We focus on reproducing basic lattice properties such as equilibrium energetics and mechanical properties as well as basic dynamic behavior described by the mean-square-displacements (MSD) of the atomic species in the structure. Our MD simulation results show excellent agreement with results obtained from DFT calculations. To date, there are no publications related to modeling AEB_6 systems in a MD setting, though numerous articles describing experimental procedures (synthesis, thermophysical properties, thermoelectric properties, etc.) or analysis of electronic structure calculations exist [11,12,14,15,17,18,22–34].

The crystal structure of MB_6 is simple cubic with octahedral space group $Pm\bar{3}m$ symmetry [3]. An octahedral unit is formed by six boron atoms located on the $6f$ $(1/2, 1/2, z)$ Wyckoff sites of the unit cell, and separate octahedra are bonded together at

[a] *Chemical and Materials Engineering Department, University of Nevada–Reno, Reno, NV 89557 USA. Fax: +1 775 784 4764; Tel: +1 775 784 6060; E-mail: victor.vasquez@unr.edu*

† To whom correspondence should be addressed.

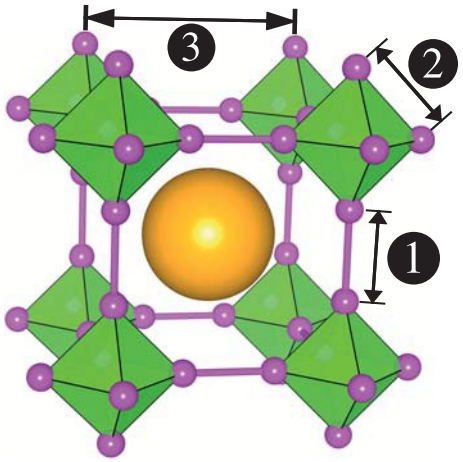

Fig. 1 General structure of metal hexaborides with central cation (orange) and boron atoms (purple). Each unit cell contains a single octahedron (eight shown) and ion. Octahedral faces are shown as green surfaces. 1 = B–B_{interO_h} bond, 2 = B–B_{intraO_h} bond, 3 = lattice constant (a).

their apexes[6] to form a three-dimensional network of covalently bonded boron atoms. The metal cation occupies the interstices of the boron framework at the $1a$ $(0, 0, 0)$ Wyckoff site[4]. Due to the symmetry of hexaborides (see Fig. 1), each unit cell of a binary hexaboride is characterized solely by the lattice constant (a) and positional parameter (z), where z is defined as

$$z = \frac{B\text{–}B_{interO_h}}{2 \cdot a} \tag{1}$$

The pronounced stability of MB_6 structures can be attributed to the covalently bonded octahedral skeleton[7,35], and elastic constants are found to depend almost entirely on the boron sublattice[36]. Formation of a MB_6 generally requires metals with first and second ionization potentials of less than 7 *eV* and 12 *eV*[37], respectively, and these two electrons are needed to produce a closed-shell configuration in the octahedral units[38,39]. For the case of divalent metals, semiconductors with energy gaps of 0.1-0.4 *eV* typically result[40], and various other properties (e.g., Pauli-paramagnetic, ferromagnetic, diamagnetic, conductive, superconductive, and complex spin-ordered states) have been found and depend on the type of cation[41].

2 Modeling Approach

Metal hexaborides and bulk metals are first modeled with DFT to perform structural optimization, obtain cohesive energy curves, and produce MSD data for hexaborides using the quasi-harmonic approximation (QHA). A lattice inversion technique and simple nearest-neighbor approach are employed to extract initial pairwise potentials from cohesive energies for bulk metals and metal-boron interactions, respectively. These are used as a guide for optimizing Morse potentials to produce the correct equilibrium data. MD simulations are then performed to modify the interactions such that they can correctly reflect MSD values, generated through DFT-QHA, at various temperatures.

2.1 Density Functional Theory

Electronic structure calculations are performed with the QUANTUM ESPRESSO integrated suite of open-source computer codes[42]. Pseudopotentials and plane-wave basis sets are used to self-consistently solve the Kohn-Sham equations. This work employs ultrasoft pseudopotentials with the generalized-gradient approximation and Perdew-Burke-Ernzerhof exchange-correlation functionals. A width of 0.02 *Ry* is given for Marzari-Vanderbilt smearing functions, and energy and electron density cut-offs are set to 80 *Ry* and 960 *Ry*, respectively. Self-consistent field calculations over the Brillouin zone use an $8 \times 8 \times 8$ Monkhorst-Pack grid for **k**-points, and thermodynamic properties derived from the QHA utilize an $8 \times 8 \times 8$ **q**-point mesh. All parameters are checked for convergence before full-scale calculations are carried out. To examine the reliability of these results, equilibrium lattice constant values for bulk α-phases of the alkaline earth metals and their respective borides have been calculated with the ultrasoft pseudopotentials and tested against published experimental data[7,43] (shown in Table 1). The MB_6 lattice constants and structural parameters have been optimized to $a_{eq} \pm 0.005$ Å and $z_{eq} \pm 0.0001$.

Table 1 Experimental and Calculated Lattice Parameters for MB_6 and Bulk Metals

	Expt		Calc	
Boride	a (Å)	z	a (Å)	z
BaB_6 †	4.2618	0.2047	4.2435	0.2046
α–Ba (BCC)‡	5.0227		5.0302	
CaB_6 †	4.1514	0.2019	4.1446	0.2018
α–Ca (FCC)‡	5.5884		5.5250	
SrB_6 †	4.1953	0.2031	4.1925	0.2032
α–Sr (FCC)‡	6.084		6.0384	

†From ref 7, ‡ From ref 43

2.2 Lattice Inversion

Assuming that pairwise interactions are sufficient to describe the cohesion within this modeling framework, the total lattice energy can be written as

$$\mathbb{E}_{tot}(a) = \sum_k \phi_k^\circ + \frac{1}{2}\sum_k \sum_i \phi_k\left(d_i^{(k)}(a)\right) \tag{2}$$

in which each sublattice "k" is represented by its isolated atomic energy ϕ_k° and a set of distances $d_i^{(k)}(a)$ dependent upon the lattice constant, a. The set $d_i^{(k)}(a)$ is fixed once a sublattice geometry is chosen, and systems which expand isotropically produce a reusable set when these displacements are normalized to the lattice constant. Counting the degeneracy at each distance, Eq. (2) can be re-written for a specific sublattice "k" as an infinite series given by

$$\mathbb{E}_k(a) = \phi_k^\circ + \frac{1}{2}\sum_{n=1}^{\infty} r_k(n) \cdot \phi_k\left(b_k(n)\, a\right) \tag{3}$$

where $\mathbb{E}_k$ refers to the total energy for sublattice "k", $r_k(n)$ is the number of atoms located in a spherical shell "n" at a distance $(b_k(n) \cdot a)$ from some reference atom, and the set $\{b_k(n)\}$ increases monotonically with "n". This relationship between pairwise inter-

action potentials and energy can be inverted through a Gaussian-type elimination procedure proposed by Carlsson, Gelatt, and Ehrenreich[44] to yield potentials as a function of the lattice energy at varying distances. For systems which exhibit a high degree of symmetry, one can alternatively employ the Chen-Möbius inversion method[45], which generates the interaction potential according to

$$\mathbb{E}_k^{coh}(a) = \frac{1}{2}\sum_{n=1}^{\infty} r_k(n)\cdot\phi_k\left(\tilde{b}_k(n)\, r_{NN}^a\right)$$

$$\Updownarrow \qquad (4)$$

$$\phi_k(r_{NN}^a) = 2\sum_{n=1}^{\infty} J_k(n)\,\mathbb{E}_k^{coh}\left(b_k(n)\,a\right),$$

where r_{NN}^a represents the nearest-neighbor distance for a particular lattice constant a, the modified distance vector $\tilde{b}_k(n)$ is given by

$$\tilde{b}_k(n) = \frac{b_k(n)\cdot a}{r_{NN}^a} \qquad (5)$$

and the values of $J_k(n)$ represent the Dirichlet inverse,

$$\sum_{b_k(m)b_k(n)=b_k(j)} J_k(n)\, r_k(m) = \delta_{j,1} \qquad (6)$$

This method has the advantage of fast convergence along with simplicity[46] and is used in this work for metal-metal potentials.

It is important to note that the inversion processes described are not valid for systems which expand anisotropically, and no method currently exists for inverting cohesive energies for these types of lattices. The metal-boron and inter-octahedral boron-boron sublattices both fall into this category. For these two, it is assumed that the first-shell of neighbors give rise to the only interactions in order to generate a suitable approximation to the curvature of the potential, and this potential is further optimized using methods described later.

3 Interatomic Potentials

3.1 Metal Homatomic Interaction

The divalent alkaline earth metals used in this work produce closed-shell configurations upon removal of two electrons to satisfy the electron requirements of the boron octahedra. It is therefore assumed that the metal-metal potentials will be sufficiently represented by a pairwise interaction. The metal sublattice within a hexaboride is easily described by a simple-cubic structure, producing a cohesive energy per atom of the form

$$\mathbb{E}_{SC}^{coh}(a) = \frac{1}{2}\sum_{(m,n,l)\neq(0,0,0)} \phi_{SC}\left(\sqrt{m^2+n^2+l^2}\,a\right) \qquad (7)$$

Initially, energy landscapes for theoretical simple cubic structures of the three metals were calculated and inverted. However, the inverted potentials gave rise to unrealistic behavior exhibiting multiple local minima, suggesting that this geometrical layout is not suitable to describe bonding within these metals. Bulk α-phases of barium, calcium, and strontium are therefore used to generate the intermetallic cohesive energies and inverted potentials, as they are the most stable at ambient temperature/pressure and should give a fairly good approximation to the correct interaction curvatures.

The face-centered cubic (FCC) phases occurring for bulk calcium and strontium have cohesive energies per atom arising from pairwise potential summations of the form

$$\mathbb{E}_{FCC}^{coh}(a) = \frac{1}{2}\sum_{(m,n,l)\neq(0,0,0)} \phi_{FCC}\left(\sqrt{m^2+n^2+l^2}\cdot a\right) + \frac{3}{2}\sum_{(m,n,l)} \phi_{FCC}\left(\sqrt{(m-1/2)^2+(n-1/2)^2+l^2}\cdot a\right) \qquad (8)$$

Alternatively, α-barium occurs in a BCC lattice with a cohesive energy per atom given by

$$\mathbb{E}_{BCC}^{coh}(a) = \frac{1}{2}\sum_{(m,n,l)\neq(0,0,0)} \phi_{BCC}\left(\sqrt{m^2+n^2+l^2}\cdot a\right) + \frac{1}{2}\sum_{(m,n,l)} \phi_{BCC}\left(\sqrt{(m-1/2)^2+(n-1/2)^2+(l-1/2)^2}\cdot a\right) \qquad (9)$$

Both of these sublattices are easily inverted using the method described in the previous section. The inversions, along with Morse potentials optimized in Sec. 4, are shown in Fig. 2 for the three metals.

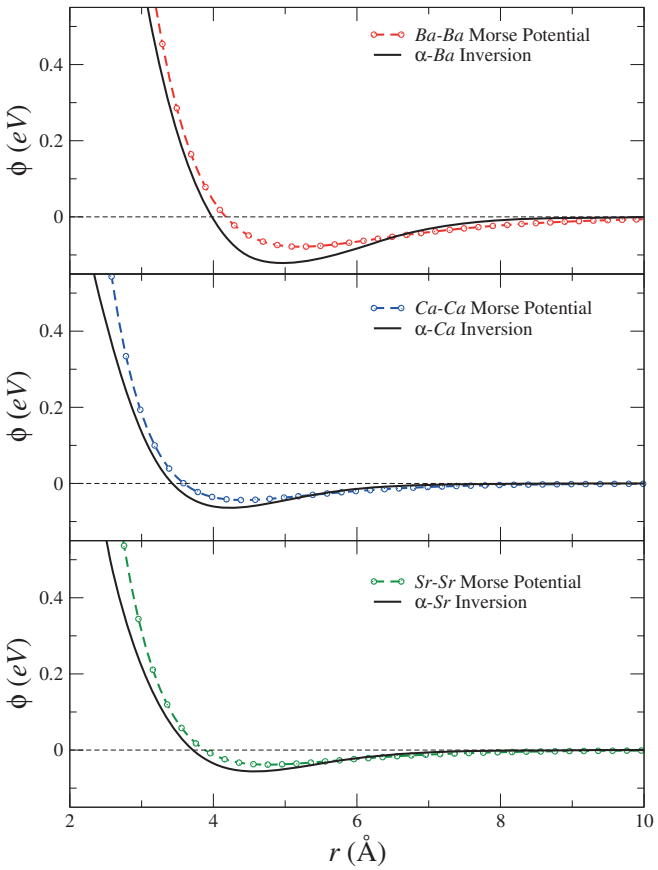

Fig. 2 Potentials for bulk α-phases of the three metals in this work obtained through inversion of cohesive energies and *Method II*.

3.2 Boron Homatomic Interaction

The boron framework is modeled in a different manner than typical non-bonded interactions. Evidence has shown that the octahedral volumes are relatively unperturbed by metal substitution[35] with variations in the interoctahedral (B–B_{interO_h}) distances being about 2.3 times greater than that of the intraoctahedral (B–B_{intraO_h}) bond lengths[7]. The homatomic boron potential is thus estimated by taking into account only B–B interactions *between* separate octahedra, keeping the octahedral volumes fixed at their calculated equilibrium values through the use of rigid B–B_{intraO_h} bonds. A similar methodology has been applied by Smith *et al.*[47] when studying lattice dynamics of MB_6. Upon analyzing Raman scattering data, Smith *et al.*[47] discovered that the internal modes of the octahedra are of such a high frequency (20-38 THz) that mixing with external modes is an unlikely event. Note that this would require MD step sizes of at maximum 2.5 fs (though probably an order of magnitude smaller to be safe) to even attempt capturing these effects, and there is doubt as to whether these high frequency vibrations would give any further insight into the macroscopic transport properties of these systems.

In order to produce a consistent set of pairwise potentials for metal hexaborides, octahedral rotational perturbations and lattice expansions are used to calculate energetics relating different geometric layouts for a lattice of rigid octahedra lacking metal cations. The $\phi^{\circ}_{B_6}$ energies are found by expanding the lattice until the variation $d\mathbb{E}/da$ has reached a minimal value, and removal of this energy is assumed to produce a cohesive energy dependent upon B–B_{interO_h} interactions only, as the intrinsic energy associated with isolated octahedrons is removed. Details of the perturbations and calculations can be found in Schmidt *et al.*[48].

3.3 Hetero-atomic Interaction

The pairwise potential approximation for non-bonded van der Waals interactions leads to the following relationship for the total system energy,

$$\mathbb{E}_{tot}(a) = \phi^{\circ}_{M} + \phi^{\circ}_{B} + \mathbb{E}_{M\cdot M}(a) + \mathbb{E}_{B\cdot B}(a) + \mathbb{E}_{M\cdot B}(a) + \mathbb{E}_{elec} \qquad (10)$$

in which the hetero-atomic interactions are given by the $\mathbb{E}_{M\cdot B}$ and $\mathbb{E}_{elec}$ energies. In ionic systems, it is common for hetero-atomic potentials to be described by a combination of an attractive Coulomb, repulsive van der Waals, and attractive van der Waals interactions, the latter generally being negligible in comparison[49]. We should therefore expect the van der Waals component of the hetero-atomic potentials to exhibit a repulsive character in nature once the electrostatic interactions have been removed.

To aid in fully characterizing the energetics encountered during dynamical motion, non-equilibrium structures are included when parametrizing the M–B potential. The system is modeled in DFT through a range of lattice constant values and translations of the metal cation within the unit cell, $(x_{M,i}, 0, 0)$, in which $x_{M,i}$ ranges from 0 to $1/2$. This isolates the M–B interaction through a range of interatomic separation distances, as the M–M and B–B sublattices are identical in all translational perturbations.

Isolation of the van der Waals potentials for the M-B interactions from the cohesive energy requires the removal of homatomic interactions and the electrostatic potential energy. The former can be calculated through a lattice summation using the interatomic potentials derived in this work. Electrostatics tend to be more complicated, though the smooth-particle mesh Ewald (SPME) offers an attractive alternative for the system sizes used in this work[50]. The use of fixed-volume octahedral units presents an additional problem, as energy calculations of rigid bodies employ different assumptions for electrostatic interactions in comparison to systems composed entirely of free atoms. A simple Coulomb potential would not have sufficed because the electrostatic energy being calculated in a MD code is not equivalent to one determined from a simple lattice summation. The calculation of electrostatics for each change in M-coordinate and lattice size is therefore handled with the SPME method in DL_POLY Classic[51]. The same parameters listed in Sec. 4.2 are used in addition to prescribing each metal cation with a $+2$ charge and boron charges $-1/3$ to give net neutrality. The advantage of using DL_POLY Classic to calculate electrostatics is that the DFT-derived cohesive energy should be recovered once all of the potentials have been placed back into a MD framework.

The cohesive energy for a M–B sublattice having fixed octahedral volumes with the M ion at the origin is given by

$$\mathbb{E}_{M\cdot B}(a) = 3\sum_{k=0}^{1}\sum_{(m,n,l)}\phi_{M\cdot B}(\Theta_{kmnl}(a)) \qquad (11)$$

with

$$\Theta_{kmnl}(a) = \left(\sqrt{\left(m+\imath^{2k}\Delta_z(a)\right)^2 + (n+1/2)^2 + (l+1/2)^2}\,a\right)$$

and

$$\Delta_z(a) = 1/2 + \left(z_{eq} - 1/2\right)\frac{a_{eq}}{a}$$

Here, a_{eq} and z_{eq} refer to the equilibrium lattice constant and positional parameter. Upon removal of the electrostatic and homatomic contributions, the van der Waals interaction between cation and boron atoms can be parametrized. As stated already, there is no method for inverting a structure with "fixed-length" unit cell parameters. An initial nearest-neighbor potential is developed assuming the cation only interacts with the first 24 equidistant nearest-neighbor boron atoms. Although this is not entirely accurate, it does provide a useful approximation for further optimization — see sections below.

4 Pairwise Potentials Parametrization

In molecular dynamics simulations, it is convenient to have pairwise interactions described by simple mathematical forms such as the Morse[52] or Buckingham[53] potentials. This convenience arises from the fact that most MD computational platforms have these and other forms already coded in their forcefields. Many MD platforms also allow the use of tables or interatomic interaction data for inputing forcefields. In principle, we could directly use the pairwise interatomic potentials obtained from the lattice inversion techniques, but we present a parametrization strategy to obtain Morse parameters from lattice inversion and cohesive

energy curves. Achieving this is not a simple task, mainly because the parameter set is expected to produce a very specific behavior — in addition to fitting the interatomic potential properly, the Morse potentials should be able to reproduce the lattice energies and MSD values for all atoms reasonably well if one wishes to capture appropriate dynamics when performing MD simulations.

For this purpose, we divide the parameter optimization approach in three stages. The first stage—*Method I*, uses lattice inversion potentials to obtain an initial set of Morse parameters that reproduce the curvature of the inversion reasonably well, within the limitations of the Morse potential model. However, different mathematical forms of potential functions have different capacities and flexibility for fitting data sets. From experience, we find that simply approximating the inversion curvature with a model potential will not suffice. Small variations in the parameter space can produce significant discrepancies in the calculation of the cohesive energies compared to those obtained from DFT calculations. The second stage—*Method II*, performs further parameter optimization to obtain a better description of the cohesive energies, while, at the same time, maintaining good predictions of the interatomic potentials. The last stage consists of performing dynamic relaxations of the system using MD simulations to further optimize the parameter set with the objective of matching the MSDs obtained from MD simulations to those obtained from DFT-QHA. The subsections below describe in more detail the overall optimization approach.

4.1 Equilibrium Energy

Morse potentials are chosen to represent the non-bonded interactions with the form

$$\phi_M(r_{ij}) = E_0\left(e^{-2k_0(r_{ij}-r_{eq})} - 2e^{-k_0(r_{ij}-r_{eq})}\right) \qquad (12)$$

where E_0 represents the dissociation energy, k_0 is related to the stiffness of the potential, and r_{eq} is the interatomic separation at which the force acting between the particles becomes null.

4.1.1 Method I

The potentials obtained for bulk metal α-phases and the metal-boron interactions from Sec. 3 provide a target function onto which a trial Morse potential can be parametrized. We chose to constrain the values for equilibrium separation, r_{eq}, and dissociation energy, E_0, of the trial Morse potential to those given by the target function, allowing optimization to occur through the parameter k_0. These values (r_{eq}, E_0) correspond to the local minimum of the target function and are easily found. An objective function defined by

$$E_{obj} = \sum_{i=0}^{N} \exp\left(-\frac{\phi_I(r_i)}{E^*}\right)\left(\phi_I(r_i) - \phi_M(r_i, r_{eq}, E_0, k_0)\right)^2 \qquad (13)$$

is then minimized for k_0. The factor E^* is a damping coefficient, $\phi_I(\cdot)$ is the target potential, $\phi_M(\cdot)$ refers to the trial Morse potential for a specific value of k_0, and i runs through all of the N data points. The form of this weighting function allows for regions of low energy to be given a greater relevance and excludes regions of very high energy, as these are not likely to be encountered. This approach is *Method I*.

4.1.2 Method II

We use *Method I* to produce an initial parameter set θ° for the Morse potential model $f_M(\mathbf{r}, \theta)$, where the parameter space is given by the array $\theta = [\mathbf{r}_{eq}, E_0, k_0]$—see Eqn. (12) for details. The initial parameter set θ° is perturbed randomly by up to $\pm 100\%$ to populate an array of potential new parameter sets $\mathbf{S}^p_\theta$, where p is the size of array—1200 in this work. These are used to compute lattice energies with potential radial cutoffs of 12 Å, and an objective function similar to *Method I*, exchanging $\phi(\cdot)$ with $\mathbb{E}(\cdot)$, allows for an error estimate between calculated cohesive energies from DFT and lattice summations. The subset $\hat{\mathbf{S}}^q_\theta \subset \mathbf{S}^p_\theta$ of size q—15 in this work, with the the lowest error in the objective function are then allowed to randomly change by $\pm 50\%$ for hundreds of iterations, keeping a new set only if the error in lattice energies has been reduced. Once a pseudo-stationary state is found, each parameter in the set is altered by $\pm 0.05\%$ while keeping the other two constant, producing 6 new parameter sets for further optimization. The change which allows for the largest decrease in error is selected, and this simple single-step searching algorithm is continued until a local optimum is found. It is common to see that a majority of the q parameter sets relax to similar stationary states of the objective function and the set with the best performance is selected as the optimal θ^*. Recalculated lattice energies for bulk metal phases can be seen in Fig. 3.

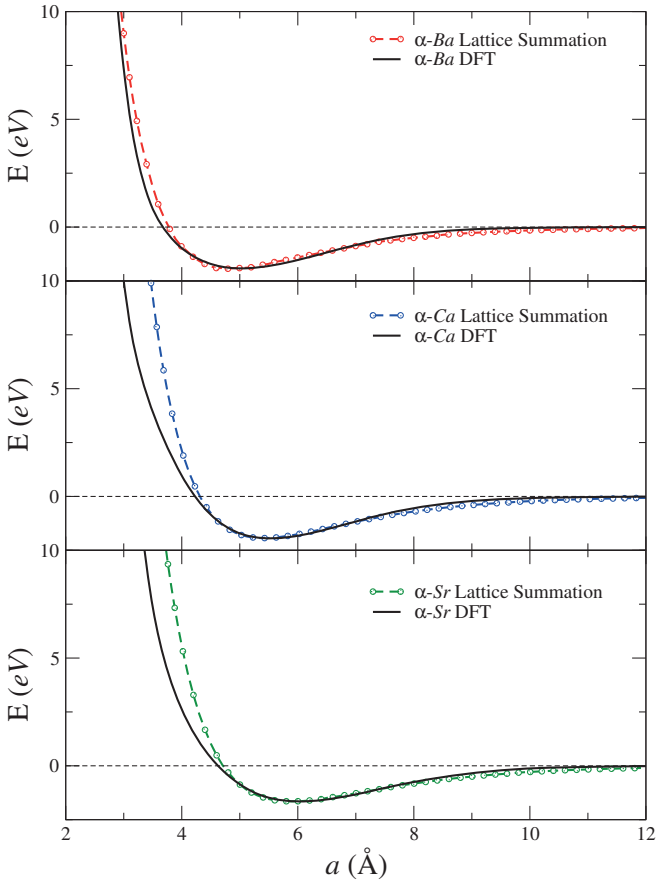

Fig. 3 Cohesive energies for bulk α-phases of the three metals used in this work from DFT and lattice summations with *Method II* potentials.

Here we can see that the attractive wells are very well approximated. Although the repulsive regions differ between the inverted and *Method II* Morse potentials, these offer a significant improvement of the *Method I* calculated cohesive energies, which are not able to predict the equilibrium lattice constants or well-depths properly.

4.2 Dynamic Relaxation

The last step of the optimization process refines the parameters to match target MSD values from the QHA results. The software package DL_POLY Classic[51] is used to perform MD calculations on an $8 \times 8 \times 8$ lattice of unit cells with equilibrated lattice parameters from DFT for each respective MB_6. The total simulation time during the optimization process is 11 ps including a 1 ps equilibration. The microcanonical ensemble uses a Nosé-Hoover thermostat with a $\tau_T = 0.5$ and is integrated with the Velocity-Verlet algorithm over 1 fs intervals. Electrostatics are calculated using the SPME method with a precision of 10^{-8}. The cut-off distance for non-bonded interactions is 12 Å to be congruent with the pair-potential development. Temperature varies between 100 K and 900 K.

An initial simulation is performed using potentials generated from *Method II* over the temperature range from $100\,K$ to $900\,K$, and MSD values are calculated from the trajectory data to give $MSD_{i,avg}(T)$ for each atom "i". Only the final 8 ps of each run is analyzed in order to mitigate any post-equilibration effects after thermostatic switching. Sample and origin intervals of 10 fs and array lengths of 4 ps are used, allowing each time point to be an average of approximately 200,000 and 1,200,000 single atom trajectories for the cation and boron, respectively. An objective function is used which incorporates the deviations in average MSD values and the slope and curvature of $MSD_{i,avg}(T)$ between MD- and DFT-calculated results. Each parameter p_j for the M–B potential is then modified by a percentage α_j, where $\alpha_j < 5$ and changes throughout the process depending on how the difference Δp_j affects the error to provide for better estimations of step sizes. Simulations are carried out for each single-parameter change $p_j \pm \Delta p_j$ over the range of temperatures, and the best-fitting parameter set is chosen to be recycled back into this process until a local minimum is found in the objective function. Constraints are additionally placed on the parameter values to favor those which minimized errors in calculated lattice energies.

The boron MSD values are given preference in the objective function with the assumption that these values should be similar in all cases. The dominant behavior of boron in providing stability to the hexaboride structure supports this claim. Experimental work by Tanaka *et al.*[36] has shown that elastic constants of a hexaboride system depends almost entirely on the boron lattice. In addition to resisting large deviations with substitution of metal cations, X-ray diffraction data of boron octahedra showed almost no change in Debye temperatures for boron octahedra with rare earth hexaborides of atomic numbers 57–61 and 63–66[54], suggesting that MSD values should also be fairly constant. Boron MSD values calculated through DFT within the QHA for four hexaborides are shown in Fig. 4 along with MD-calculated displacements for the LaB_6[48] system. Note that the oscillation amplitudes for LaB_6 from MD nearly capture the entire range of values for the four hexaborides. Using the hetero-atomic potentials for optimization, Table 2 shows the finalized parameters for each system.

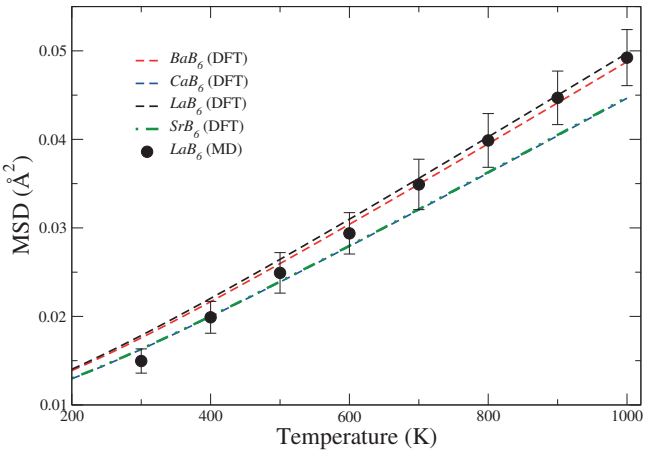

Fig. 4 Calculated boron MSDs from DFT and MD for four hexaboride structures.

Table 2 Finalized Parameters for Interatomic Morse Potentials with Alkaline-Earth Hexaborides

Interaction	M Charge	r_{eq} (Å)	E_0 (eV)	k_0 (Å^{-1})
Ba–Ba	+2	5.2070	0.07833	0.6690
Ba–B	+2	3.8964	0.06655	1.3142
Ca–Ca	+2	4.4104	0.04349	0.8432
Ca–B	+2	3.8431	0.08011	1.2287
Sr–Sr	+2	4.7578	0.03824	0.7914
Sr–B	+2	3.8034	0.09163	1.2628
B–B	+2	1.5160	2.21657	2.5688

5 Results

5.1 Mean-Square Displacements

The three metal hexaboride systems are simulated at $50\,K$ and between $100\,K$ and $1000\,K$ at $100\,K$ intervals in DL_POLY Classic. All parameters for performing simulations aside from simulation times are given in Sec. 4.2. Each run is carried out for 50 ps, which includes a 10 ps equilibration period. The final 40 ps are used to calculate MSDs for both atom types with array lengths of 5 ps and sample and origin intervals of 10 fs. An example of the hexaboride MSDs is given for BaB_6 to show similarities between MD- and DFT-calculated values in Fig. 5. To allow for comparison, results for boron and cations within each hexaboride structure can be found in Fig. 6 and Fig. 7, respectively. Note that these values are normalized to MSD values generated by QUANTUM ESPRESSO.

The boron MSD values all follow the same pattern, predicting displacements more accurately as temperature is increased. The deviations in the lower temperature regions are believed to be the result of quantum effects, and can be explained from a simple argument on the principles of molecular dynamics. Zero-point

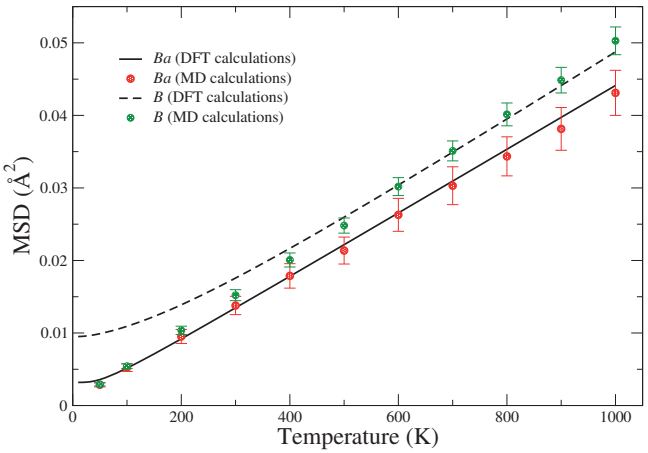

Fig. 5 Barium and boron MSD values for BaB_6 calculated within MD and DFT-QHA.

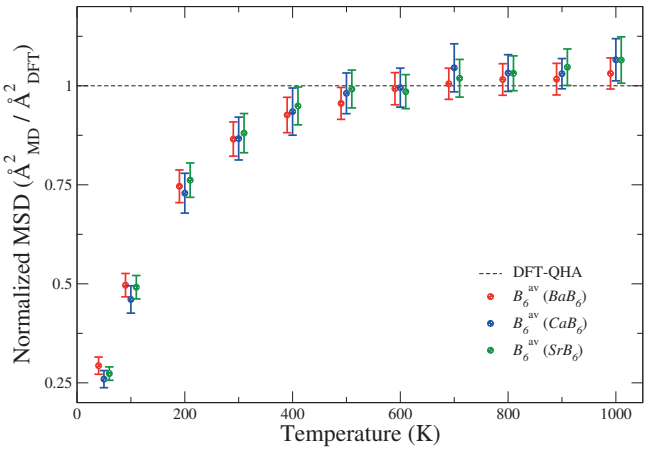

Fig. 6 Boron MSD values for BaB_6, CaB_6, and SrB_6. Values and deviations are normalized to DFT values for each system. Temperature values for BaB_6 and SrB_6 have been shifted from the correct (CaB_6) values to reflect differences.

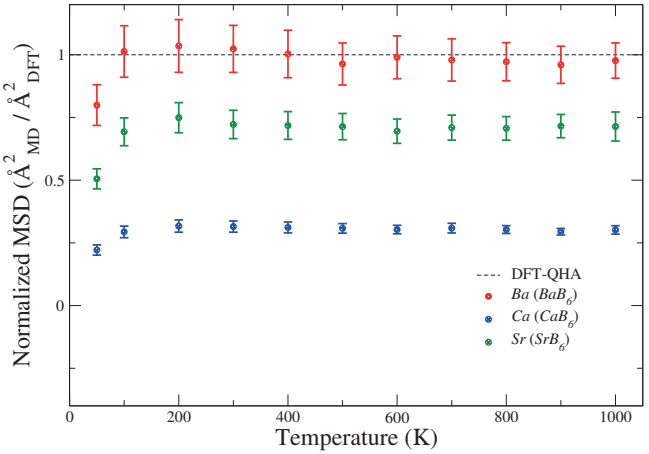

Fig. 7 Cation MSD values for BaB_6, CaB_6, and SrB_6. Values and deviations are normalized to DFT values for each system.

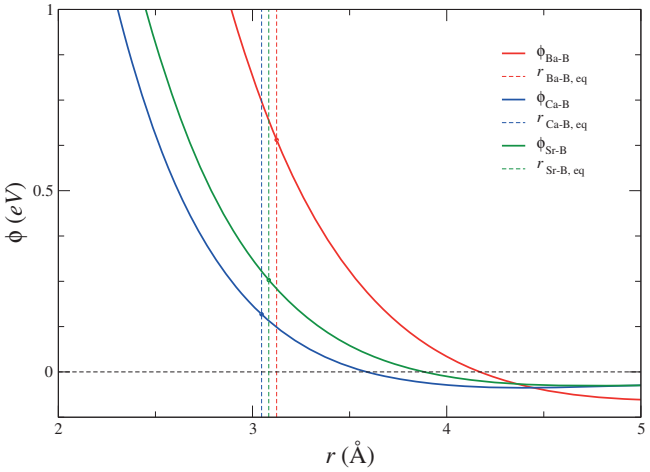

Fig. 8 Metal-boron potentials developed in this work (solid lines) and equilibrium M–B contact distances (dotted lines).

motion (ZPM) is a quantum mechanical effect which cannot manifest itself in a classical framework based upon the solution of the Newtonian equations of motion. The ZPM is more pronounced for the smaller boron atoms, and the magnitude of these low temperature displacements has been found neccesary to correctly predict the thermodynamic stability of bulk boron[55]. The error in this region is therefore unavoidable, as classical motions should always drop off at zero temperature.

The three metals are seen to follow the correct trends with regard to the relationship between thermal kinetic energy and displacements, the predictions being very well for barium and decreasing in accuracy with atomic size. This appears to be an added effect of the M–B and B–B potentials. The B–B interaction was developed by parametrizing a Morse potential to accurately reflect the equilibrium energetics and MSD values, owing to the fact that there are currently no appropriate methods to invert cohesive energies for systems with anisotropic lattice expansions. It has been found that a Morse potential which reproduces the correct lattice energies generally has the same shape but a smaller and more dispersed energy well than the corresponding inverted potential. This effect can be seen in Fig. 2 for the metal-metal potentials. If one assumes that the B–B interaction follows the same relationship, a larger value of E_0 and k_0 would give rise to a more stable boron cage whose motion is less susceptible to metal contact.

In addition, we believe that the size of the metal-boron contact distance has a stabilizing effect on the octahedral lattice, allowing a weak B–B bond to be sufficient in damping thermal motion of the boron atoms. To illustrate the point, metal-boron potentials for the three atoms are shown in Fig 8. The equilibrium contact distances and associated energies for each atom correctly appear to decrease with decreasing size and molecular weight, but there is a constant repulsion between the boron and metal ions. This forces the motion of any metal ion around its equilibrium position to exponentially increase the system's configurational energy unless both atom types move synchronously, a result which acts to favor states with similar displacements and is observed here. A stronger B–B interaction would allow for smaller M–B r_{eq} values and hence a lower resistance to asymmetric displacements. Uncoupling the MSDs should not have any detrimental effects, as

displacements tend to increase with decreasing mass and balance the effective momentum felt by the octahedra.

The choice to fit MSD values favoring boron displacements came with a loss in accuracy for the metal MSDs but also provides insight into how the potentials can be improved. At the end of each optimization step using MD (Sec. 4.2), a 40 *ps* simulation is performed with the optimal parameter set from that step to evaluate the accuracy and stability of MSDs generated during the 11 *ps* simulation. This not only serves as an indication of whether the system has fully equilibrated, but gives an illustration of the independence between the motions of the two atom types as the parameters are modified. Analysis of the MSDs from these 40 *ps* simulations shows a trend in the relationship between cation and boron MSDs – as the MSD for one atom type increased, the other appeared to do so proportionally. Therefore, the only way to increase the lower molecular weight atom MSD values would be to also increase boron MSDs, giving further evidence that the atoms in these systems were not nearly as independent as they need to be to create the profiles found from *ab initio* data.

5.2 Cohesive Energy

Electrostatics calculated via the SPME method are used in conjunction with lattice summations to produce cohesive energy curves for the three systems. These are shown along with DFT calculations in Fig. 9. These results are reasonable for the equilibrium structures and energies. It is worthwhile to note that the majority of non-electrostatic cohesive energy near the equilibrium lattice constant comes from the B–B bonding energies; therefore, deviations from the equilibrium values are expected to be small. These can be observed in Table 3, where the calculated equilibrium cohesive energies and lattice constants are shown for pair-potential (PP) lattice summations and DFT-calculations. The error in lattice constants is always less than 1% and cohesive energy errors seem to increase with decreasing ion size, though they are fairly accurate given the amount of non-equilibrium data used during parametrization. The trends in Fig. 9 indicate that a portion of the attractive well (a = 4.5 – 9 Å) is not accounted for within this model. This is probably due to the use of the electrostatics calculated with the SPME. It is known that the majority of cohesion in ionic crystals is due to electrostatic interactions[56], forcing the cohesive energy to be heavily dependent on the form of this potential. When using SPME in DL_POLY Classic, the non-bonded radial cutoff r_{cut} = 12 Å is not incorporated in the electrostatic calculation to avoid discontinuities in the force. Rather than tapering off to zero at r_{cut}, the Coulomb potential has a fairly large and constant slope for the entire range. In order to produce a more accurate represenation of the lattice energy in this ionic system, one would benefit from alternative methods for electrostatic calculations which incorporate smoothing functions and radial cutoffs. An example of this is the method proposed by Wolf *et al.*[57].

5.3 Mechanical Properties

To investigate how the change in curvature between the classical model and *ab initio* calculations affects the mechanical properties of the three materials investigated, the bulk modulus B_o is calculated for each of the six cohesive energy curves, using the Murnaghan equation of state[58] to determine the value of B_o. We note that the use of fixed octahedra will have some effect on the actual values, but the errors are expected to be small—the variation in inter-octahedral boron-boron bond lengths is much larger than intra-octahedral bonds. This fact supports the idea that the inter-octahedral bonds will provide less resistance to compression and expansion; therefore, a majority of the bond-length deformations are expected in these bonds. The calculated bulk moduli can be found in Table 4 for DFT and lattice summations using the current pair-potentials. The three AEB_6 systems show similar trends in the errors between DFT and lattice summation values for B_o and errors given in Table 3, having better agreement for larger cations. A published experimental value of 169.9 *GPa* for the bulk modulus of CaB_6 has been determined through X-ray diffraction

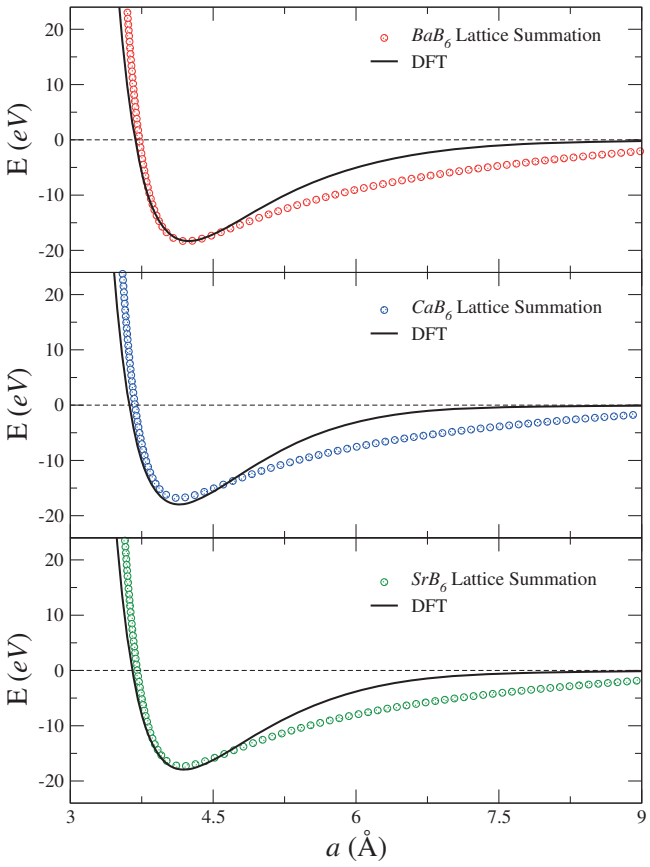

Fig. 9 Cohesive energies for each of the three systems modeled from DFT-calculations and lattice summations using the SPME for electrostatics.

Table 3 Equilibrium Lattice Values for MB_6 from DFT and Current Model

	Lattice Constant, a			Cohesive Energy, $\mathbb{E}$		
Crystal	DFT (Å)	PP (Å)	Err (%)	DFT (eV)	PP (eV)	Err (%)
BaB_6	4.2435	4.2198	0.558	−18.313	−18.338	0.137
CaB_6	4.1446	4.1370	0.183	−17.965	−16.801	6.479
SrB_6	4.1925	4.1766	0.379	−17.933	−17.309	3.480

Note: PP = Pair Potentials, Err = $|1-(\mathrm{PP}/\mathrm{DFT})|$

Table 4 Bulk Moduli Calculated from Murnaghan EOS for MB_6 from DFT and Current Model

Crystal	DFT (*GPa*)	PP (*GPa*)	Err (%)
BaB_6	152.680	140.128	8.22
CaB_6	168.377	140.263	16.70
SrB_6	160.265	140.561	12.29

Note: PP = Pair Potentials, Err = $|1 - (PP/DFT)|$

studies[59], in excellent agreement with our DFT calculations. Unfortunately, experimental data is sparse in the academic literature for the mechanical properties of these systems, so comparison is mainly limited to *ab initio* calculations. Theoretical calculations of B_o were found for BaB_6[60] (162 *GPa*), CaB_6[60–62] (147.83–159 *GPa*), and SrB_6[60,63] (149.87–160 *GPa*), which are in agreement with the values obtained from both DFT calculations and the classical model used in this work.

6 Conclusions

In this work, we developed a modeling framework for metal hexaborides to estimate inter-atomic pair potentials for use in molecular dynamics simulations. The framework uses a combination of the DFT and MD techniques to obtain pairwise potentials that can be readily applied to the analysis of atomic movement in these type of materials. Mean square displacements (MSD) and equilibrium energetics can be predicted fairly very well for calcium, barium, and strontium hexaborides. The metal-boron potentials seem to work better for larger cations such as Ba and Sr. For calcium, the deviations between calculated MSDs from MD and QHA estimations are larger.

In the neighborhood of the equilibrium regions, the cohesive energies estimated with the pair potentials developed in this work are in excellent agreement with those estimated from DFT calculations. This is important and required if one wants to capture appropriate dynamic behavior of these materials in a molecular dynamics setting. Additionally, the modeling framework proposed provides better insight on the nature of the atomic interactions in these crystals. Using rigid body dynamics for the octahedral units reduces the complexity significantly of using molecular dynamics to study these materials at larger scales than those typical of DFT calculations.

7 Acknowledgments

We gratefully acknowledge funding support from NSF Award No. 1246792 (“SNM: Scalable Manufacturing of Unique Hexaboride Nanomaterials for Advanced Energy Generation and Gas Storage Applications”). Fig. 1 was created in part using the software package VESTA[64].

References

1 P. Lemis-Petropoulos, V. Kapaklis, A. Peikrishvili and C. Politis, *Int. J. Mod. Phys. B*, 2003, **17**, 2781–2788.
2 U. Mukherji, *Engineering Physics*, Alpha Science Intl Ltd, Oxford, 2006.
3 P. Loboda, H. Kysla, S. Dub and O. Karasevs'ka, *Mater. Sci.*, 2009, **45**, 108–113.
4 L. Bai, N. Ma and F. Liu, *Phys. B (Amsterdam, Neth.)*, 1009, **404**, 4086–4089.
5 S. Kimura, T. Nanba, M. Tomikawa, S. Kunii and T. Kasuya, *Phys. Rev. B.: Condens. Matter Mater. Phys.*, 1992, **46**, 12196–12204.
6 J. Lafferty, *J. Appl. Phys.*, 1951, **22**, 299–309.
7 C.-H. Chen, T. Aizawa, N. Iyi, A. Sato and S. Otani, *J. Alloys Compd.*, 2004, **366**, L6–L8.
8 X. Guo-Liang, C. Jing-Dong, X. Yao-Zheng, L. Xue-Feng, L. Yu-Fang and Z. Xian-Zhou, *Chin. Phys. Lett.*, 2009, **26**, 156201.
9 V. Craciun and D. Craciun, *Appl. Surf. Sci.*, 2005, **247**, 384–389.
10 S. Ordan'yan, Y. Paderno, E. Nikolaeva and I. Khoroshilova, *Powder Metall. Met. Ceram.*, 1984, **23**, 387–389.
11 A. Aprea, A. Maspero, A. F. Albisetti and G. Giunchi, *Solid State Sci.*, 2012, **14**, 1587–1590.
12 S. Amin, S. you Li, J. Roth and T. Xu, *Chem. Mater.*, 2009, **21**, 763–770.
13 M. Gürsoy, M. Takeda and B. Albert, *J. Solid State Chem.*, 2015, **221**, 191–195.
14 X. Huang, J. Zhong, L. Dou and K. Want, *Int. J. Refract. Met. Hard Mater.*, 2010, **28**, 143–149.
15 J. Xu, Y. Zhao, C. Zou and Q. Ding, *J. Solid State Chem.*, 2007, **180**, 2577–2580.
16 B. Galanov, V. Kartuzov, O. Grigoriev, L. Melakh, S. Ivanov, E. Kartuzov and P. Swoboda, *Procedia Eng.*, 2013, **58**, 328–337.
17 M. Takeda, M. Terui, N. Takahashi and N. Ueda, *J. Solid State Chem.*, 2006, **179**, 2823–2826.
18 S. Zhou, J. Zhang, L. Bao, X. Yu, Q. Hu and D. Hu, *J. Alloys Compd.*, 2014, **611**, 130–134.
19 K. Maiti, V. Medicherla, S. Patil and R. Singh, *Phys. Rev. Lett.*, 2007, **99**, 266401.
20 K. Maiti, *Europhys. Lett.*, 2008, **82**, 67006.
21 L. Chao, L. Bao, J. Shi, W. Wei, O. Tegus and Z. Zhang, *J. Alloys Compd.*, 2015, **622**, 618–621.
22 K. Schmitt, C. Stückl, H. Ripplinger and B. Albert, *Solid State Sci.*, 2001, **3**, 321–327.
23 G. Min, S. Zheng, Z. Zou, H. Yu and J. Han, *Mater. Lett.*, 2003, **57**, 1330–1333.
24 Z.-G. Li, C.-G. Piao, X. Pan, Y.-K. Wei, Y. Cheng and G.-F. Ji, *Physica B (Amsterdam, Neth.)*, 2012, **407**, 361–367.
25 T. Jarlborg, *Physica B (Amsterdam, Neth.)*, 2001, **307**, 291–302.
26 Y. Imai, M. Mukaida, M. Ueda and A. Watanabe, *Intermetallics*, 2001, **9**, 721–734.
27 I. Kang and C. Park, *J. Korean Phys. Soc.*, 2006, **49**, S490–S494.
28 B. Lee and L.-W. Wang, *Appl. Phys. Lett.*, 2005, **87**, 262509.
29 H. Ripplinger, K. Schwarz and P. Blaha, *J. Solid State Chem.*, 1997, **133**, 51–54.
30 Y. Jiao, F. Wang, X. Hong, W. Su, Q. Chen and F. Zhang, *Phys. Lett. A*, 2013, **377**, 823–827.

31 H. Kino, F. Aryasetiawan, K. Terakura and T. Miyake, *Phys. Rev. B.: Condens. Matter Mater. Phys.*, 2002, **66**, 121103.

32 S. Massidda, A. Continenza, T. de Pascale and R. Monnier, *Z Phys B*, 1997, **102**, 83–89.

33 R. Kanakala, R. Escudero, G. Rojas-George, M. Ramisetty and O. Graeve, *ACS Appl. Mater. Interfaces*, 2011, **3**, 1093–1100.

34 R. Kanakala, G. Rojas-George and O. Graeve, *J. Am. Ceram. Soc.*, 2010, **93**, 3136–3141.

35 C. Oshima, M. Umeuchi and T. Nagao, *Surf. Sci.*, 1993, **298**, 450–455.

36 T. Tanaka, J. Yoshimoto, M. Ishii, E. Bannai and S. Kawai, *Solid State Commun.*, 1977, **22**, 203–205.

37 N. Greenwood, R. Parish and P. Thornton, *Q. Rev., Chem. Soc.*, 1966, **20**, 441–464.

38 H. Longuet-Higgins and M. de V Roberts, *Proc. R. Soc. London, Ser. A*, 1954, **224**, 336–347.

39 C. Börrnert, Y. Grin and F. Wagner, *Z. Anorg. Allg. Chem.*, 2013, **639**, 2013–2024.

40 R. Johnson and A. Daane, *J. Chem. Phys.*, 1963, **38**, 425–432.

41 T. Lundström, *Pure Appl. Chem.*, 1985, **57**, 1383–1390.

42 P. Giannozzini, S. Baroni, N. Bonini, M. Calandra, R. Car, C. Cavazzoni, D. Ceresoli, G. Chiarotti, M. Cococcioni, I. Dabo, A. Corso, S. de Gironcoli, S. Fabris, G. Fratesi, R. Gebauer, U. Gerstmann, C. Gougoussis, A. Kokalj, M. Lazzeri, L. Martin-Samos, N. Marzari, F. Mauri, R. Mazzarello, S. Paolini, A. Pasquarello, L. Paulatto, C. Sbraccia, S. Scandolo, G. Sclauzero, A. Seitsonen, A. Smogunov, P. Umari and R. Wentzcovitch, *J. Phys.: Condens. Matter*, 395502, **21**, 2009.

43 H. King, in *CRC Handbook of Chemistry and Physics*, ed. D. Lide, CRC Press, Boca Raton, FL, 87th edn, 2005, ch. Crystal Structures and Lattice Parameters of Allotropes of the Elements.

44 A. Carlsson, C. Gelatt and H. Ehrenreich, *Philos. Mag. A*, 1980, **41**, 241–250.

45 N.-X. Chen and G. bao Ren, *Phys. Rev. B.: Condens. Matter Mater. Phys.*, 1992, **45**, 8177–8180.

46 N.-X. Chen, *Möbius Inversion in Physics*, World Scientific, New Jersey, 2010.

47 H. Smith, G. Dolling, S. Kunii, M. Kasaya, B. Liu, K. Tekegahara, T. Kasuya and T. Goto, *Solid State Commun.*, 1985, **53**, 15–19.

48 K. Schmidt, O. Graeve and V. Vasquez, *J. Phys. Chem. C*, 2015, **119**, 14288–14296.

49 C. Kittel, *Introduction to Solid State Physics*, John Wiley & Sons, New York, 2005.

50 D. Frenkel and B. Smit, *Understanding Molecular Simulation: From algorithms to applications*, Academic Press, San Diego, 2002.

51 W. Smith, T. Forester and I. Todorov, *The DL_POLY Classic User Manual*, STFC Daresbury Laboratory, Cheshire, UK, 1st edn, 2010.

52 P. Morse, *Phys. Rev.*, 1929, **34**, 57–64.

53 R. Buckingham, *Proc. R. Soc. London, Ser. A*, 1938, **168**, 264–283.

54 V. Novikov, *Phys. Solid State*, 2003, **45**, 1469–1474.

55 M. van Setten, M. Uijttewaal, G. de Wijs and R. de Groot, *J. Am. Chem. Soc.*, 2007, **129**, 2458–2465.

56 N. Ashcroft and N. Mermin, *Solid State Physics*, Harcourt College, New York, 1976.

57 D. Wolf, P. Keblinski, S. Phillpot and J. Eggebrecht, *J. Chem. Phys.*, 1999, **110**, 8246–8253.

58 F. Murnaghan, *Am. J. Math.*, 1937, **59**, 235–260.

59 M. Li, W. Yang, L. Li, H. Wang, S. Liang and C. Gao, *Physica B (Amsterdam, Neth.)*, 2011, **406**, 59–62.

60 G. Grechnev, A. Baranovskiy, V. Fil, T. Ignatova, I. Kolobov and A. Logosha, *Low Temp. Phys.*, 2008, **34**, 921–929.

61 Y. Wei, J. Yu, Z. Li, Y. Cheng and G. Ji, *Physica B (Amsterdam, Neth.)*, 2011, **406**, 4476–4482.

62 A. Liu, X. Zhang and Y. Qiao, *Ceram. Int.*, 2014, **40**, 15997–16002.

63 Z. Li, C. Piao, X. Pan, Y. Wei, Y. Cheng and G. Ji, *Physica B (Amsterdam, Neth.)*, 2012, **407**, 361–367.

64 K. Momma and F. Izumi, *J. Appl. Crystallogr.*, 2011, **44**, 1272–1276.

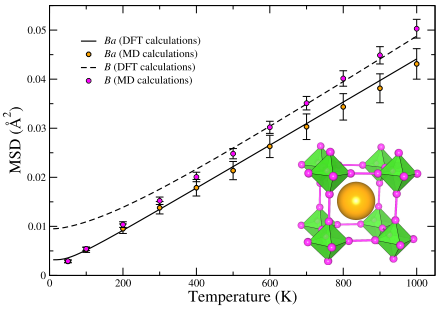

Pairwise potentials are developed using DFT and MD methods for a new model to describe energies and dynamics in alkaline-earth hexaborides.